Check for updates

Tunable angle-dependent electrochemistry at twisted bilayer graphene with moiré flat bands

Yun Yu [1], Kaidi Zhang[1], Holden Parks[2], Mohammad Babar[2], Stephen Carr [3],
Isaac M. Craig [1], Madeline Van Winkle[1], Artur Lyssenko[1], Takashi Taniguchi [4], Kenji Watanabe [5],
Venkatasubramanian Viswanathan [2,6] and D. Kwabena Bediako [1,7] ✉

Tailoring electron transfer dynamics across solid–liquid interfaces is fundamental to the interconversion of electrical and chemical energy. Stacking atomically thin layers with a small azimuthal misorientation to produce moiré superlattices enables the controlled engineering of electronic band structures and the formation of extremely flat electronic bands. Here, we report a strong twist-angle dependence of heterogeneous charge transfer kinetics at twisted bilayer graphene electrodes with the greatest enhancement observed near the 'magic angle' (~1.1°). This effect is driven by the angle-dependent tuning of moiré-derived flat bands that modulate electron transfer processes with the solution-phase redox couple. Combined experimental and computational analysis reveals that the variation in electrochemical activity with moiré angle is controlled by a structural relaxation of the moiré superlattice at twist angles of <2°, and 'topological defect' AA stacking regions, where flat bands are localized, produce a large anomalous local electrochemical enhancement that cannot be accounted for by the elevated local density of states alone.

In electrochemical reactions, the flow of charge from electrode to electrolyte drives chemical transformations at the interface, and such interfacial electron transfer reactions underpin key technologies that interconvert electrical and chemical energy[1–5]. Advances in the development of atomically thin, so-called two-dimensional (2D) materials have provided distinctive avenues for controlling interfacial charge transfer and surface reactivity[6,7] due to their electronic properties that are exceptionally manipulable by subtle structural modifications[8–12] and other external electrostatic perturbations[13]. Specifically, defects and edge sites present at 2D surfaces are recognized as reactive hot spots in interfacial charge transfer processes owing to their modified electronic properties[7]. However, the small areal fraction of edge sites[14] constrains the maximized utilization of the whole surface. In addition, it is generally challenging to achieve rational control of atomic defects[10] and an optimized selectivity[15] of the defect-induced enhancement.

Atomic layers that are 2D are also the building blocks for the design of artificial van der Waals (vdW) materials through the deterministic assembly of multiple layers[16]. These vdW heterostructures possess weak interlayer interactions that allow arbitrary azimuthal orientations ('twist angles') between the 2D lattices to be independently controlled, introducing a unique degree of freedom for modulating the electronic properties of 2D materials[17,18]. Recent work has discovered an extraordinarily wide and growing collection of exotic physics in twisted 2D layers[19–23]. For example, twisting a graphene bilayer from a Bernal (AB) stacking configuration to a 'magic angle' of ~1.1° results in the formation of electronic bands with very weak dispersion in momentum space (so-called 'flat' bands)[24,25]. This recent work on twisted graphene as well as twisted atomic layers of transition metal compounds[26] has shown

that these flat bands produce an array of intertwined correlated electronic phases, including correlated insulating states[20,26], unconventional superconductivity[19,21,23] and orbital magnetism[22,23]. In twisted 2D materials such as these, a form of 'topological' defects is formed at the intersection between different stacking domains[27]. Apart from hosting low-temperature correlated-electron physics, these topological defects are conceptually analogous to structural atomic defects that generate localized states that can impact interfacial charge transfer chemistry. While a handful of studies interrogating the effects of interlayer twist on chemical reactivity have been reported[28–30], these experiments have been restricted to large twist angles (≥7°) well outside the flat band and 'magic angle' regime. The possibility of exploiting this concept of moiré flat bands and topological defects to modulate interfacial charge transfer rates has therefore remained unexplored.

Here, we probe the kinetics of a heterogeneous electron transfer reaction at well-defined twisted bilayer graphene (TBG) surfaces and show that the kinetics can be strongly tailored by the interlayer moiré twist angle, θ_m, at small angles ($0.22° \leq \theta_m \leq 5°$). In TBG, the azimuthal misorientation between two homologous layers creates an in-plane quasiperiodic modulation in the crystallographic registry, revealed as a moiré superlattice pattern that displays alternating regions of AA, AB/BA and saddle-point (SP) stacking configurations (Fig. 1a)[31–33]. The periodicity of the moiré supercells, also known as the moiré wavelength, λ_m, and the size of the mini-Brillouin zone of the moiré superlattice (Fig. 1b) are both highly dependent on θ_m. Hybridization between adjacent Dirac cones results in an electronic band structure that is strongly modified by the twist angle[20,24] as shown in Fig. 1c for 'magic angle' TBG ($\theta_m = 1.1°$). At this θ_m, the bands around 0 eV become remarkably flat, creating a massively

[1]Department of Chemistry, University of California, Berkeley, CA, USA. [2]Department of Mechanical Engineering, Carnegie Mellon University, Pittsburgh, PA, USA. [3]Brown Theoretical Physics Center, Brown University, Providence, RI, USA. [4]International Center for Materials Nanoarchitectonics, National Institute for Materials Science, Tsukuba, Japan. [5]Research Center for Functional Materials, National Institute for Materials Science, Tsukuba, Japan. [6]Department of Physics, Carnegie Mellon University, Pittsburgh, PA, USA. [7]Chemical Sciences Division, Lawrence Berkeley National Laboratory, Berkeley, CA, USA. ✉e-mail: bediako@berkeley.edu
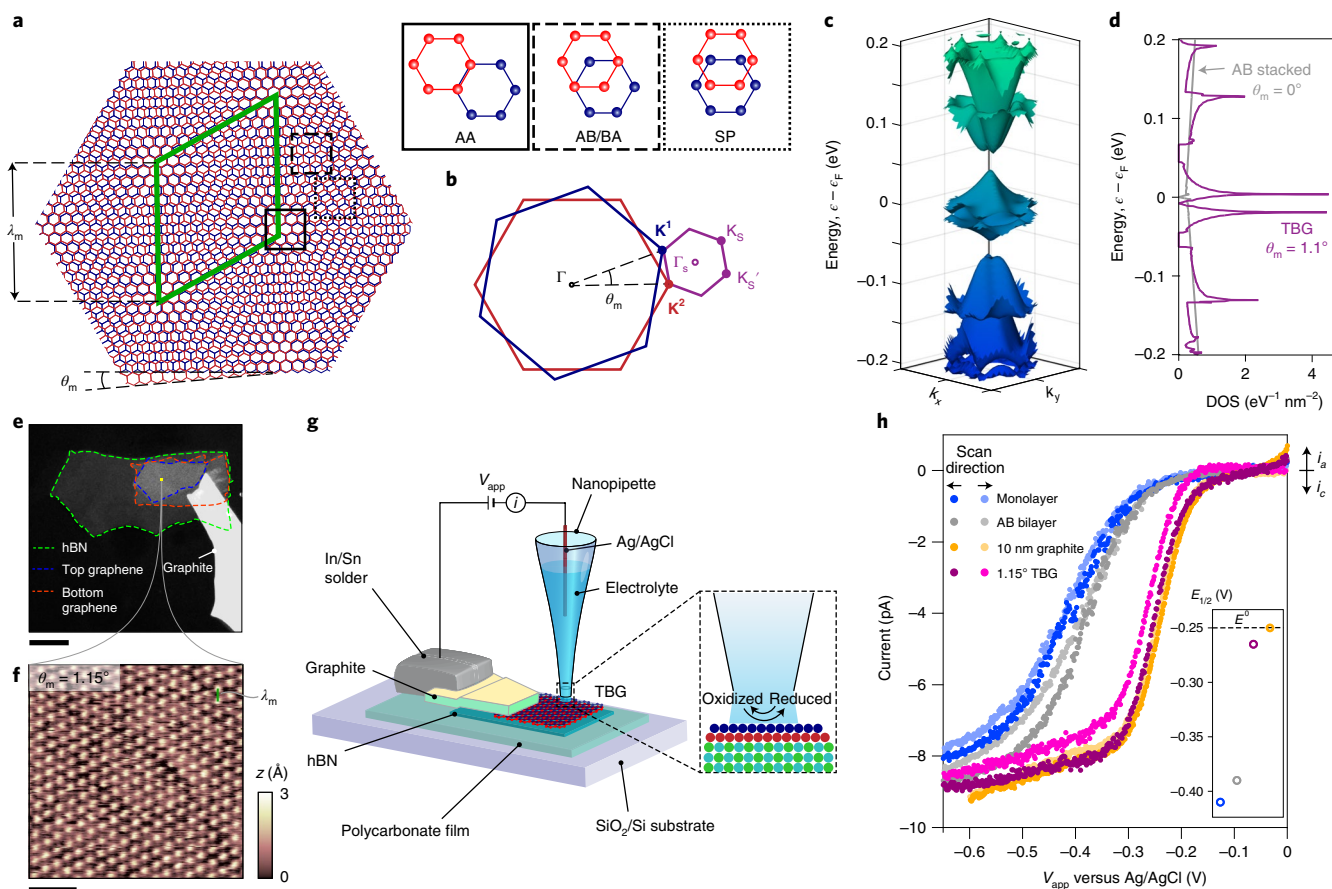
Fig. 1 | Twisted bilayer graphene moiré superlattices and their electrochemical response. a, Schematic of the three stacking configurations (AA, AB/BA and SP) and a moiré pattern in TBG with a moiré wavelength, $\lambda_m = a/[2\sin(\theta_m/2)]$, where $a = 2.46$ Å is the lattice constant of graphene. **b**, The mini-Brillouin zone of a TBG superlattice generated from the difference between two wavevectors ($\mathbf{K}^1$ and $\mathbf{K}^2$). **c,d**, Calculated moiré band (**c**) of 1.1° TBG and corresponding DOS (**d**). ϵ_F, Fermi energy. k_x and k_y are the reciprocal space vectors. **e**, Optical image of a TBG/hBN heterostructure connected to a graphite contact. Scale bar, 10 μm. **f**, Constant-current STM image of 1.15° TBG acquired from the region marked with a yellow dot in **e**, showing λ_m for one moiré supercell. Scale bar, 50 nm. z, height. **g**, Schematic of local voltammetric measurement at a TBG surface in a SECCM set-up equipped with a single-channel nanopipette probe (diameter, ~100 nm). **h**, Representative steady-state voltammograms of 2 mM Ru(NH$_3$)$_6^{3+}$ in 0.1 M KCl solution obtained at separate, freshly prepared graphene monolayer (blue), Bernal-stacked bilayer (grey), 10-nm-thick graphite (orange) and 1.15° TBG (purple). Scan rate, 100 mV s^{-1}. The inset shows the half-wave potentials of each cyclic voltammogram compared to E^0. i_a and i_c represent anodic and cathodic currents, respectively.

enhanced electronic density of states (DOS) concentrated within a narrow energy range of ~20 meV (Fig. 1d)[20,24]. At larger θ_m, the bands become more dispersive, with increasing bandwidths and higher energies associated with the locations of the van Hove singularities (Extended Data Fig. 1). As we now show, these moiré flat-band-originated DOS enhancements at van Hove singularities play a critical role in governing the heterogenous electron transfer rate at a graphene–electrolyte interface, making θ_m a descriptor of the interfacial reaction kinetics. We also demonstrate that spatially localized moiré flat bands allow the reaction kinetics to be precisely tuned by the topological defect (AA stacking) density, which is modulated as a function of θ_m.

Results and discussion

Interfacial electrochemistry at magic angle graphene. We fabricated hexagonal boron nitride (hBN)-supported TBG samples with controlled interlayer twist angles in the range of 0.22–5.1° (Methods for details). Figure 1e shows an optical micrograph of a TBG/hBN sample in contact with a graphite flake as the electrical contact. Figure 1f shows a typical constant-current scanning

tunnelling microscopy (STM) image of an exemplary TBG/hBN sample displaying a clear moiré superlattice pattern as observed previously[32]. For ultraclean TBG surfaces such as these, the strong electronic localization of flat bands in real space makes it possible to visualize the AA sites as elevated spots, while AB/BA and SP sites appear lower in STM topography[32,34]. The twist angle and uniaxial heterostrain are measured by geometric analysis (Methods) of the local moiré superlattice patterns obtained from STM maps that are collected from multiple arbitrary locations in each sample (Supplementary Figs. 2–4). This random sampling approach is used to ensure reasonably uniform local twists throughout a TBG sample (Supplementary Fig. 5) prior to electrochemical measurements.

Scanning electrochemical cell microscopy (SECCM)[14,15,35,36] with ~100 nm spatial resolution allows us to obtain electrochemical measurements exclusively at the basal plane of TBG (Fig. 1g). A quartz nanopipette (Supplementary Fig. 6) filled with 2 mM hexaammineruthenium(III) chloride and 100 mM aqueous potassium chloride is used to make meniscus contact with the sample surface, creating a confined electrochemical cell in which localized voltammetry is performed at a series of locations. Typical
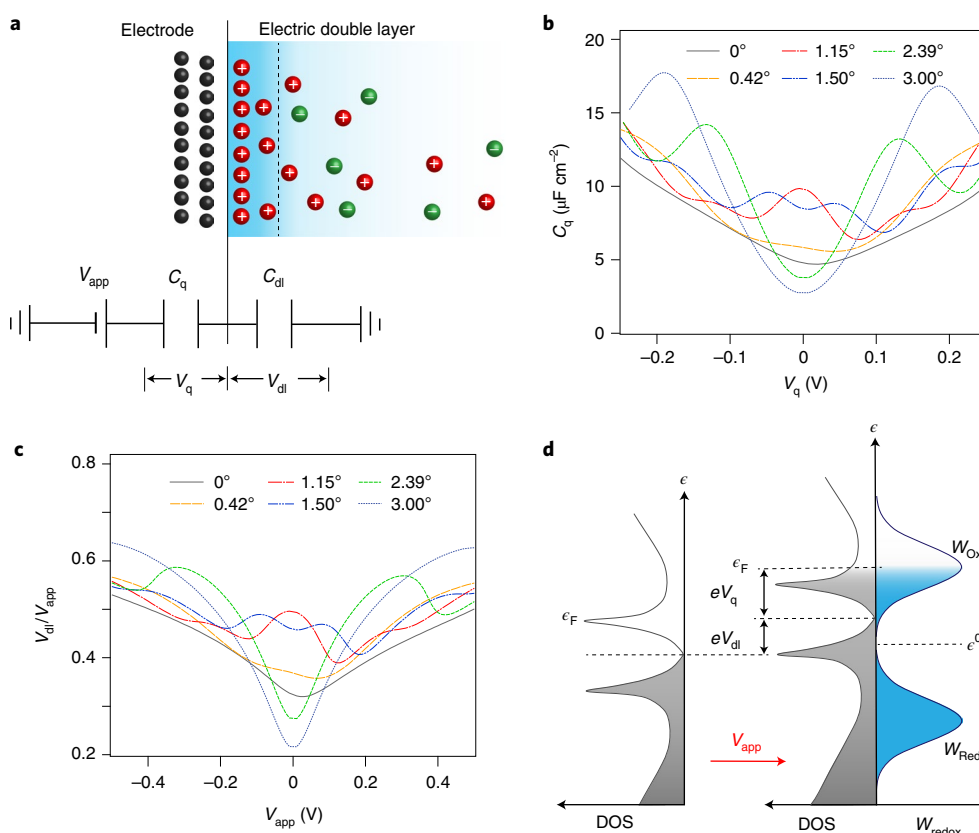
Fig. 2 | Quantifying quantum capacitance effects in interfacial electron transfer in TBG. a, Schematic of the electrode–electrolyte interface represented as the double-layer capacitance (C_{dl}) in series with the chemical quantum capacitance (C_q). **b**, Calculated C_q as a function of the chemical potential (V_q) for various twist angles. **c**, Calculated potential drop on the double layer (V_{dl}) as a function of the applied potential (V_{app}) for various twist angles. V_q and V_{app} are relative to the charge neutrality potential. **d**, Energy diagram depicting interfacial charge transfer with the consideration of electrode DOS and relative contributions of V_{dl} and V_q. W_{redox} is the probability distribution function of the solution-phase molecule (W_{Ox}, oxidized form; W_{Red}, reduced form).

steady-state voltammograms of $Ru(NH_3)_6^{3+}$ reduction obtained at the basal planes of hBN-supported monolayer graphene, Bernal (AB)-stacked bilayer graphene, 10-nm-thick graphite (~30 layers) and 1.15° TBG are shown in Fig. 1h. The anodic shift of the half-wave potential, $E_{1/2}$, with increasing graphene thickness is consistent with the electroreduction of $Ru(NH_3)_6^{3+}$ proceeding more rapidly with augmented DOS from increasing numbers of layers[14]. Remarkably, the 1.15° TBG shows a massive enhancement in reaction kinetics, approaching that of graphite, notwithstanding that it consists of only two graphene layers, and exhibiting nearly electrochemically reversible behaviour at the basal plane of this atomically thin electrode.

Quantum capacitance and interfacial charge transfer model. Applying an electric potential (V_{app}) across a solid–solution interface results in the formation of an electrical double layer adjacent to the solid surface, which serves to screen the excess charge[37,38]. At low-dimensional materials like graphene, the charged ions of the double layer also act cumulatively as an effective electrostatic 'gate' that shifts the Fermi level, ϵ_F, relative to the band edges of the material via dynamic electron/hole doping. Consequently, a considerable fraction of V_{app} is consumed as a change of the chemical potential (V_q), while the remainder is confined in the electric double layer (V_{dl}). The contribution from V_q is modelled by introducing an additional capacitance, the so-called quantum capacitance (C_q)[39,40], in series with the double-layer capacitance (C_{dl}) as shown in Fig. 2a. To evaluate C_q in TBG, we computed electronic band structures for TBG over a range of θ_m (Methods) and determined theoretical

C_q values as a function of V_q in each case. Figure 2b shows that higher values of C_q near the charge neutrality point are observed in TBG for $1° < \theta_m < 2°$, suggesting that a lower fraction of V_{app} would be spent on C_q in TBG around these values of θ_m due to an enhanced DOS near ϵ_F. Figure 2c shows how V_{dl}/V_{app} evolves as a function of V_{app} as θ_m is tuned. Higher values of V_{dl}/V_{app} are also observed near charge neutrality for $1° < \theta_m < 2°$, consistent with the angle dependence of C_q in Fig. 2b. These results show how moiré-derived flat bands can promote bulk metal-like behaviour (increased C_q and higher V_{dl}/V_{app}) in low-dimensional electrodes.

To consider the impact of partitioning V_{app} into V_q and V_{dl} in the electrochemistry of TBG, we turn to the Gerischer–Marcus[37,38] or Marcus–Hush–Chidsey formalism with the consideration of electrode DOS[41,42]. In this framework, the outer-sphere electron transfer rate constant, k_{red} (for an electroreduction reaction) is the integral of the overlap between the electronic states of the electrode and those of the solution-phase molecule at all energies (ϵ). When we include considerations brought about by a finite C_q, k_{red} can be modelled as

$$k_{red} = \nu \int_{-\infty}^{+\infty} \epsilon_{red}(\epsilon) D(\epsilon - eV_{dl}) f(\epsilon - eV_{app}) W_{Ox}(\epsilon) d\epsilon \quad (1)$$

$$W_{Ox} = (4\pi\lambda k_B T)^{-1/2} e^{\frac{-(\epsilon - \epsilon^0 - \lambda)^2}{4\lambda k_B T}} \quad (2)$$

where ν is the integral prefactor that considers the strength of the electronic interactions between the reactant and electrode, $\epsilon_{red}(\epsilon)$
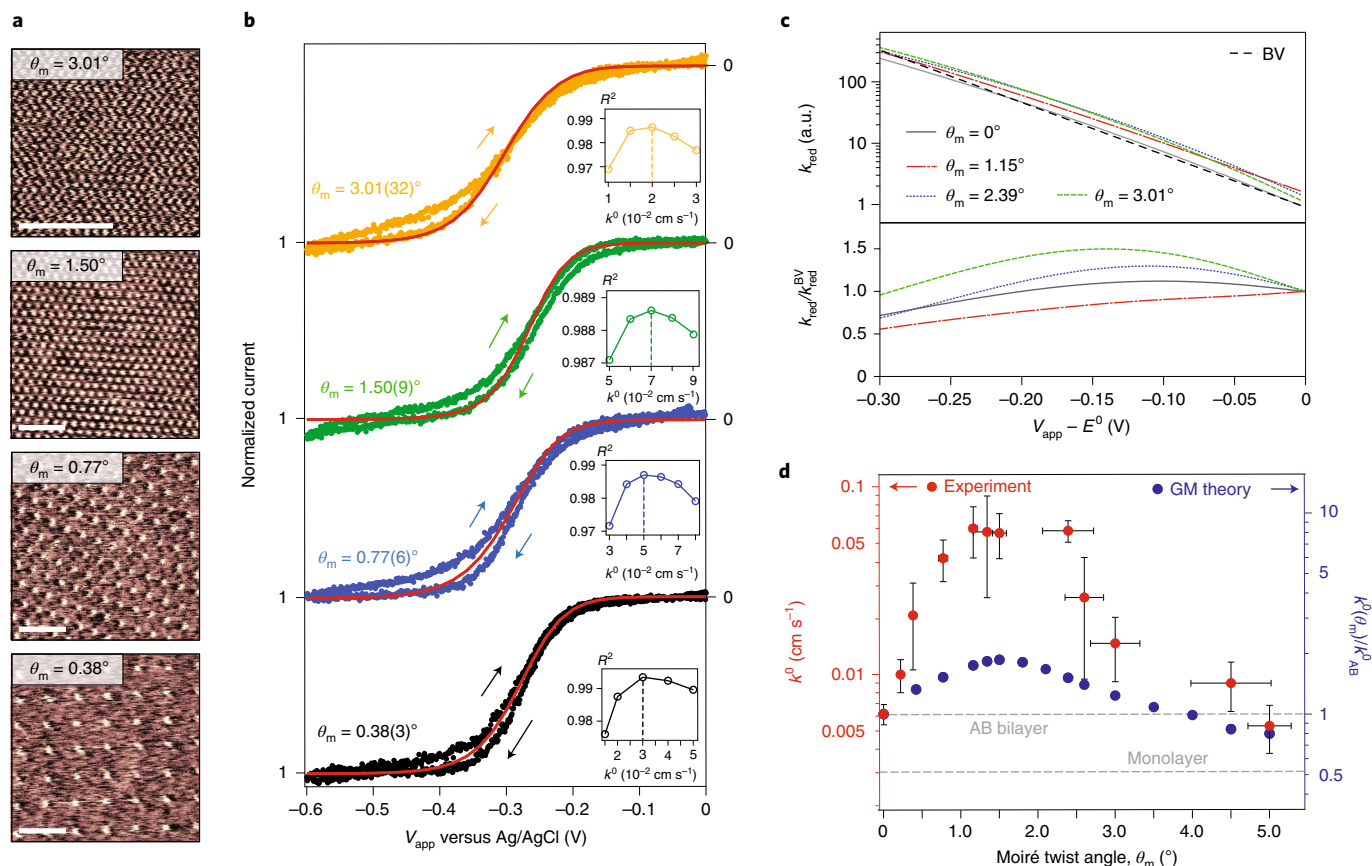
Fig. 3 | Moiré angle-dependent electron transfer rate. a, Constant-current STM images of TBG with $\theta_m = 0.38°$, $0.77°$, $1.5°$ and $3°$. Scale bars, 50 nm. **b**, Representative steady-state voltammograms of 2 mM Ru(NH$_3$)$_6$$^{3+}$ in 0.1 M KCl solution obtained in TBG with $\theta_m = 0.38°$, $0.77°$, $1.5°$ and $3°$. The current versus potential curves were normalized to the mass transfer limiting current. The simulated voltammograms are depicted by solid red lines, and the insets display the coefficient of determination (R^2 values) from comparisons of experimental voltammograms to simulated curves. Scan rate = 100 mV s^{-1}. **c**, Top, k_{red} versus V_{app} dependence for different θ_m calculated with Gerischer–Marcus (GM) framework compared to the trend of the BV model ($\theta_m = 0°$). Bottom, potential-dependent prefactor, $A(V_{app}) = k_{red}/k_{red}^{BV}$. **d**, Standard rate constants (k^0) extracted from the experimental voltammograms as a function of twist angle compared to the theoretical values normalized to the calculated value at $\theta_m = 0°$. Each red dot denotes the mean value of the k^0 values obtained from a series of measurements at one sample. The horizontal and vertical error bars represent the standard deviations of θ_m and k^0, respectively.

is the proportionality function, $D(\epsilon)$ is the DOS of the electrode, e is the elementary charge, $f(\epsilon)$ is the Fermi–Dirac function, $W_{Ox}(\epsilon)$ is the normalized probability distribution representing the electronic states of the reactant, λ is the reorganization energy, k_B is the Boltzmann constant, T is the temperature and ϵ^0 is the energy corresponding to the standard potential, E^0. In Fig. 2d, we consider the result of applying a potential bias V_{app} across the solid–electrolyte interface. In this case, ϵ_F is shifted by eV_q relative to the band edge, while eV_{dl} shifts the entire band relative to the energy of the redox molecule. This means that ultimately, the energetic alignment of electron donor–acceptor states is affected by the relative contributions from V_{dl} and V_q, and k_{red} is governed by $D(\epsilon)$ near ϵ_F. Since $D(\epsilon)$ is controlled by θ_m, this analysis predicts that k_{red} should display a dependence on θ_m.

Angle-dependent electrochemical kinetics. Figure 3 and Supplementary Fig. 7 examine the aforementioned expectation of a dependence of k_{red} on θ_m. TBG samples with a range of θ_m (representative STM images are shown in Fig. 3a) are used to measure steady-state voltammograms of Ru(NH$_3$)$_6$$^{3+}$ reduction. Based on the established model for voltammetric SECCM experiments[14], we performed finite-element simulations of the characteristic voltammetric responses (Supplementary Section 1) to extract the standard rate constant, k^0, from the experimental cyclic voltammetry data.

This kinetic parameter k^0 denotes the intrinsic electron transfer rate defined in the Butler–Volmer (BV) formulation[38]:

$$k_{red}^{BV} = k^0 e^{-\alpha \frac{F}{RT}(V_{app} - E^0)} \qquad (3)$$

where k_{red}^{BV} is the rate constant for the reduction reaction derived from the BV model, α is the transfer coefficient (Supplementary Section 1), R is the molar gas constant and F is the Faraday constant. In our analysis, we consider two key effects that arise from the effects of variable $C_q(V_q)$ with θ_m that were discussed in Fig. 2.

We first explicitly account for diffuse double-layer effects involving the migration of charged species in the diffuse layer, which would in turn affect the voltammetric response[43,44] (Supplementary Section 1). Second, we introduce a potential-dependent prefactor $A(V_{app})$ to the BV equations to account for the possibility of changing DOS with V_{app}. We determine $A(V_{app})$ by integrating the convolution of $D(\epsilon)$, $f(\epsilon)$ and $W_{Ox}(\epsilon)$ over all energies to obtain theoretical k_{red} values as a function of V_{app} for each θ_m (Fig. 3c, top). We then compare these k_{red} values to those derived from the BV model with a constant prefactor, such that $A(V_{app}) = k_{red}/k_{red}^{BV}$ (Fig. 3c, bottom). Figure 3c shows that the theoretical k_{red} values that are derived from the Gerischer–Marcus model can be reasonably fit by the BV model with a constant prefactor for small overpotentials ($V_{app} - E^0 < 0.2$ V). Nevertheless, we still apply this small correction for the potential
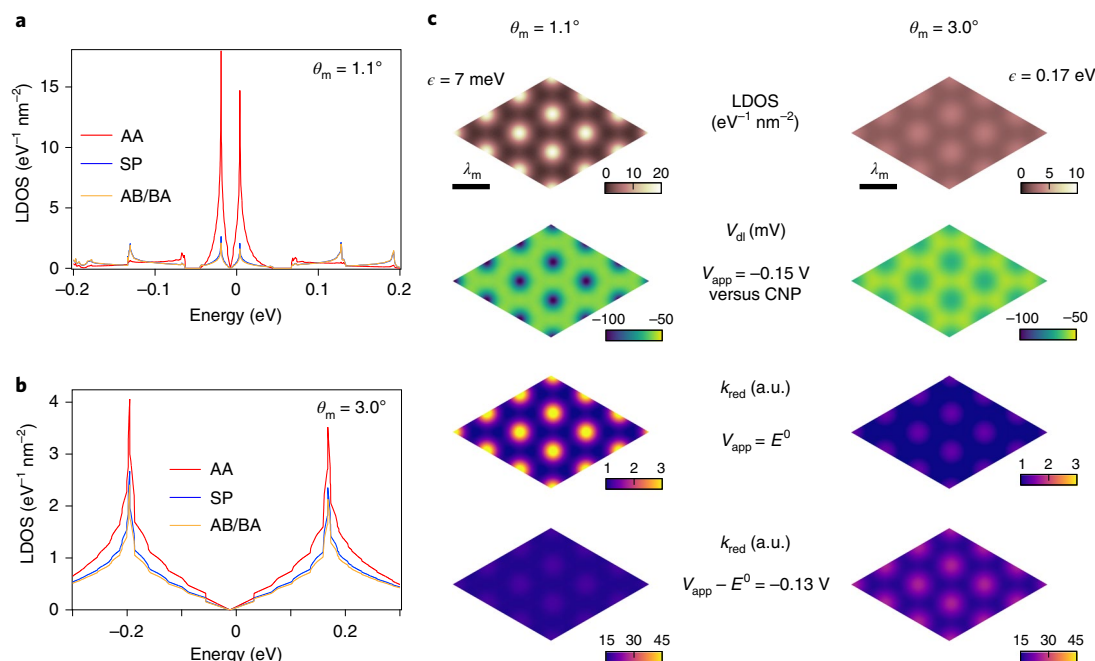
Fig. 4 | Theoretical electron transfer kinetics within a TBG moiré unit cell. a–b, Calculated LDOS versus energy at AA, AB/BA and SP in TBG of $\theta_m = 1.1°$ (**a**) and 3.0° (**b**). **c,** Calculated real-space maps of LDOS, V_{dl} and k_{red} for TBG of $\theta_m = 1.1°$ (left column) and 3.0° (right column). The LDOS are mapped at the energy corresponding to the van Hove singularities of each angle. The V_{dl} values are calculated at $V_{app} = -0.15$ V versus charge neutrality potential (CNP). Maps of k_{red} are shown at lower overpotential (third row) and higher overpotential (fourth row). The scale bars represent the length of λ_m.

dependence of the apparent rate constant in BV equations (also Supplementary Fig. 8).

Figure 3d shows the resultant dependence of k^0 on θ_m extracted from the experimental voltammograms (red markers; also Supplementary Fig. 9e and Supplementary Table 1). As implied by the voltammograms in Fig. 1h, we find the k^0 extracted from TBG for $0.8° < \theta_m < 2°$ is strongly enhanced over that of Bernal (AB)-stacked bilayer graphene ($\theta_m = 0°$). In comparison to Bernal bilayer graphene, there is minimal enhancement of k^0 for $\theta_m > 4°$, and for $\theta_m < 1°$, k^0 decreases monotonically with θ_m. We attribute the enhancement of k^0 between $\theta_m = 0.8°$ and $\theta_m = 2°$ to the elevated DOS arising from the flattened bands that are energetically matched with the formal potential of $Ru(NH_3)_6^{3+/2+}$ (Extended Data Fig. 2c). Our assertion on the criticality of energy matching with the flat bands in dictating the enhanced electron transfer kinetics in TBG was tested by electrochemical measurements with ferrocenemethanol (FcMeOH) and tris(1,10-phenanthroline)cobalt(II), $Co(Phen)_3^{2+}$, which possess formal potentials that are poorly aligned with the charge neutrality point of graphene and, for that matter, the flat bands of small angle ($\theta_m < 2°$) TBG (Extended Data Fig. 2c). For FcMeOH$^{+/0}$, inherently facile kinetics leads to nearly reversible voltammetric responses of FcMeOH (refs. [14,36]) at all θ_m values (Supplementary Fig. 10). However, the intrinsically slow kinetics of $Co(Phen)_3^{3+/2+}$ allowed us to extract rate constants from the voltammograms obtained at various θ_m values (Supplementary Fig. 11), revealing a considerably weaker dependence of k^0 on θ_m compared with that of $Ru(NH_3)_6^{3+/2+}$ (Extended Data Fig. 3). These results are consistent with our expectation for energetically misaligned donor–acceptor electronic states involving the flat bands; the electrochemical kinetics are not substantially dependent on the electronic flat band.

Figure 3d also shows the theoretical dependence of k^0 for $Ru(NH_3)_6^{3+/2+}$ on θ_m (blue markers) calculated from the Gerischer–Marcus model (equations (1) and (2)), manifesting a qualitatively consistent trend. The maximum enhancement is predicted between $\theta_m = 1.2°$ and $\theta_m = 1.6°$, where the optimal combination of large DOS and energy match is achieved after incorporating the effects of quantum capacitance. For $\theta_m > 2°$, the positions of van Hove singularities become further apart from E^0, the magnitude of DOS gradually decays and k^0 diminishes as a result. While qualitatively descriptive of the experimental data, interestingly, these calculations greatly underestimate the enhancement due to flattened bands in the range $0° < \theta_m < 3°$. To explain the anomalous enhancement of k^0 at low twist angles as well as the observed monotonic decrease in k^0 with decreasing θ_m for $\theta_m < 1°$, we evaluated the experimental and theoretical real-space variations in k^0 throughout the moiré superlattice.

Spatial variation in electrokinetics at graphene moiré superlattices. The electronic flat band formed in TBG moiré superlattices is strongly localized in real space. The local DOS (LDOS) versus energy at the three stacking regions (AA, AB/BA and SP) in 'magic angle' TBG ($\theta_m = 1.1°$) is shown in Fig. 4a. These calculations show how the prominent enhancement of DOS near charge neutrality is strongly localized at AA sites with much lower DOS found at AB/BA or SP stacking sites, in agreement with previous studies[32,34]. By contrast, Fig. 4b shows a very weak real-space partitioning of the overall DOS in TBG with $\theta_m = 3°$, where flat bands are largely absent. These localization effects can also be visualized in the real-space LDOS maps shown in Fig. 4c. Importantly, because of DOS localization, the interfacial properties of moiré superlattice electrodes are also strongly modulated in real space. Specifically, Fig. 4c also shows that the potential drop across the double layer (V_{dl}) should be nearly uniform in real space over the moiré structure for $\theta_m = 3°$, whereas V_{dl} would be concentrated at AA sites for $\theta_m = 1.1°$ due to higher LDOS and C_q. Similarly, these calculations predict an enhancement of the electroreduction rate constant, k_{red}, for $Ru(NH_3)_6^{3+/2+}$ at AA sites near zero overpotential ($V_{app} = E^0$). As the overpotential increases, ϵ_F shifts over the flat band due to the charging of C_q. The enhancement effects from the flat band are diminished at high overpotentials
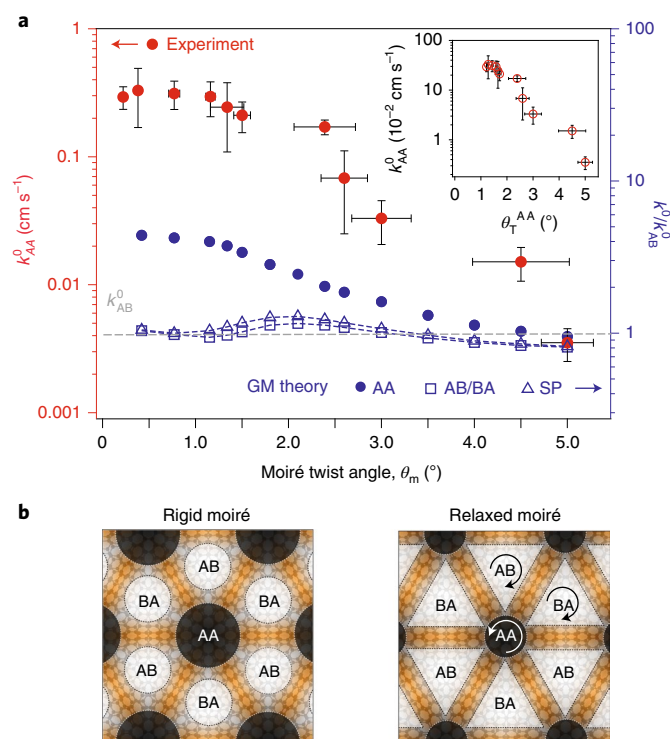
Fig. 5 | Lattice relaxation and anomalous enhancement of electron transfer kinetics at AA regions of TBG. a, Experimental local k^0 at AA sites as a function of θ_m extracted from Fig. 3d compared to the theoretically predicted (GM) values of k^0 at AA, AB/BA and SP stacking regions. The horizontal and vertical error bars represent the standard deviations of θ_m and k^0_{AA}, respectively. The inset shows the local k^0 at AA sites as a function of θ_T^{AA}. **b**, Schematic illustration of the lattice relaxation process.

($V_{app} - E^0 = -0.13\,V$), leading to a uniform k_{red} distribution across the moiré unit cell. For $\theta_m = 3°$, the calculated maps of k_{red} show minimal spatial variation over all potentials, as expected.

We extract the experimental local k^0 values for AA stacking regions (k^0_{AA}) from the ensemble k^0 measured in the meniscus covering multiple moiré unit cells. To do so, we take advantage of the independently measurable rate constant for AB stacking (k^0_{AB}), which is determined from standalone measurements at AB bilayers (that is, $\theta_m = 0°$; Fig. 1h and Fig. 3d). Considering the ensemble current as arising from the sum of local currents weighted by the area fraction, γ, of each domain (AA, AB/BA and SP), the ensemble rate constant, k^0, may be written as

$$k^0 = \gamma_{AA}k^0_{AA} + \gamma_{AB}k^0_{AB} + \gamma_{SP}k^0_{SP} \quad (4)$$

where k^0_{AA}, k^0_{AB} and k^0_{SP} denote the respective local rate constants at the AA, AB/BA and SP domains. To simplify the analysis, we assume $k^0_{AB} \approx k^0_{SP}$, a reasonable approximation given the very similar LDOS calculated (Fig. 4a–c) and measured by STM (Fig. 3b)[32]. These considerations reduce equation (4) to

$$k^0 = \gamma_{AA}k^0_{AA} + (1 - \gamma_{AA})k^0_{AB} \quad (5)$$

To determine area fraction values for equation (5), we have previously employed four-dimensional scanning transmission electron microscopy[33] to reveal that γ_{AA} increases monotonically with θ_m until θ_m reaches ~2° due to a spontaneous lattice relaxation process involving localized rotations[31,33,45], after which area fractions approach values expected from a rigid moiré (Supplementary Fig. 13). These insights allow us to extract experimental values for k^0_{AA} as a

function of θ_m in Fig. 5a. Interestingly, we find that k^0_{AA} is insensitive to twist angle for $\theta_m < 1.5°$, showing a constant value around $0.2\,cm\,s^{-1}$. This trend is fully consistent with our previous structural measurements[33] that unveiled the geometric effects of lattice relaxation (Fig. 5b). At $\theta_m < 1.5°$, positive local rotations centred on the AA stacking sites cause the atomic geometry in these regions to be nearly insensitive to the global θ_m, 'pinning' the local rotation to ~1.2°. On the other hand, localized negative rotation in AB/BA regions produces a local atomic geometry that closely matches Bernal-stacked bilayer graphene[33]. Thus, our measurements show that for $\theta_m < 1.5°$, the primary effect that drives the θ_m-dependent ensemble k^0 shown in Fig. 3d is the change in the attendant AA stacking area fraction, whereas the local electrochemical activities remain effectively constant (plateau in k^0_{AA} for $\theta_m < 1.5°$ in Fig. 5a). This convergence of local electrochemical behaviour is also manifest in plots of k^0_{AA} as a function of the net local AA rotation after lattice relaxation, θ_T^{AA} (inset of Fig. 5a). At larger θ_m, the enhancement from flat bands and the lattice relaxation process both diminish, causing k^0_{AA} to eventually become similar to k^0_{AB} for $\theta_m \geq 4°$. As a result, k^0_{AA} exhibits a monotonic downward trend with the increase of the local and global moiré angle at AA sites (inset of Fig. 5a).

While this local θ_m dependence is qualitatively supported by the theoretical values that are plotted in parallel with the experimental values in Fig. 5, we find a large discrepancy between the experimental k^0_{AA} values and those calculated using the Gerischer–Marcus model alone (also Supplementary Fig. 14). Crucially, Fig. 5 reveals that the discrepancy between theory and experiment in overall k^0 (Fig. 3d) originates from this underestimation in k^0_{AA} specifically (Fig. 5a). Further, this large, anomalous enhancement of the electron transfer rate cannot be explained merely by the commensurability of energetic overlap between donor–acceptor states, nor by the enhanced DOS (Fig. 2d). Instead, we suggest that this observation may be explained by modifications to the electronic coupling strength (ν in equation 1) with θ_m. It is reasonable to expect that the highly localized flat bands in small angle TBG (Fig. 4c), analogous to the localized electronic edge states at zigzag graphene edges[36,46], would result in substantially larger real-space overlap of the electronic wavefunctions of the TBG and solution-phase redox complexes, inducing an additional augmentation of the measured rate. Additionally, it is conceivable that greater local double-layer potentials (higher local V_{dl} in Fig. 4c) at AA sites could also modify the structure of the electric double layer and/or create a shorter electron tunnelling distance between the electrode and redox species through electro-osmosis and/or stronger electrostatic interactions with the charged complexes, and thus induce a transition to the adiabatic regime[38]. Additional theoretical and experimental studies may shed light on the origin of this anomalous enhancement.

Conclusions

The intriguing interfacial electron transfer behaviour of TBG demonstrated here suggests that in addition to low-temperature correlated electronic phases, moiré-derived flat bands in vdW architectures present a distinctively tunable material platform to systematically manipulate and fundamentally probe interfacial charge transfer and (electro)chemical transformations at well-defined surfaces. In lieu of introducing foreign dopants or structural defects that can be difficult to control, we have demonstrated the feasibility of activating the pristine graphene basal plane surface with topological defects that originate from the structural symmetry breaking in twisted bilayers[27]. We show that by the precise control of the interlayer twist angle, flat bands that are intrinsically localized to nanoscale domains in real space may be exploited to tailor the rate constant for an outer-sphere charge transfer reaction. We anticipate that flat-band engineering with moiré architectures will become a general strategy to tune the chemical reactivity of a variety of 2D surfaces beyond graphene.

Online content

Any methods, additional references, Nature Research reporting summaries, source data, extended data, supplementary information, acknowledgements, peer review information; details of author contributions and competing interests; and statements of data and code availability are available at https://doi.org/10.1038/s41557-021-00865-1.

References

1. Marcus, R. A. Electron transfer reactions in chemistry: theory and experiment (Nobel Lecture). *Angew. Chem. Int. Ed.* **32**, 1111–1121 (1993).
2. Seh, Z. W. et al. Combining theory and experiment in electrocatalysis: insights into materials design. *Science* **355**, eaad4998 (2017).
3. Hwang, J. et al. Perovskites in catalysis and electrocatalysis. *Science* **358**, 751–756 (2017).
4. Boettcher, S. W. & Surendranath, Y. Heterogeneous electrocatalysis goes chemical. *Nat. Catal.* **4**, 4–5 (2021).
5. Grimaud, A., Hong, W. T., Shao-Horn, Y. & Tarascon, J.-M. Anionic redox processes for electrochemical devices. *Nat. Mater.* **15**, 121–126 (2016).
6. Deng, D. et al. Catalysis with two-dimensional materials and their heterostructures. *Nat. Nanotechnol.* **11**, 218–230 (2016).
7. Jin, H. et al. Emerging two-dimensional nanomaterials for electrocatalysis. *Chem. Rev.* **118**, 6337–6408 (2018).
8. Chia, X. & Pumera, M. Characteristics and performance of two-dimensional materials for electrocatalysis. *Nat. Catal.* **1**, 909–921 (2018).
9. Jaramillo, T. F. et al. Identification of active edge sites for electrochemical H_2 evolution from MoS_2 nanocatalysts. *Science* **317**, 100–102 (2007).
10. Zhong, J. H. et al. Quantitative correlation between defect density and heterogeneous electron transfer rate of single layer graphene. *J. Am. Chem. Soc.* **136**, 16609–16617 (2014).
11. Wang, L. et al. Tunable intrinsic strain in two-dimensional transition metal electrocatalysts. *Science* **363**, 870–874 (2019).
12. Li, H. et al. Activating and optimizing MoS_2 basal planes for hydrogen evolution through the formation of strained sulphur vacancies. *Nat. Mater.* **15**, 48–53 (2016).
13. Wang, Y., Udyavara, S., Neurock, M. & Frisbie, C. D. Field effect modulation of electrocatalytic hydrogen evolution at back-gated two-dimensional MoS_2 electrodes. *Nano Lett.* **19**, 6118–6123 (2019).
14. Güell, A. G. et al. Redox-dependent spatially resolved electrochemistry at graphene and graphite step edges. *ACS Nano* **9**, 3558–3571 (2015).
15. Mariano, R. G., McKelvey, K., White, H. S. & Kanan, M. W. Selective increase in CO_2 electroreduction activity at grain-boundary surface terminations. *Science* **358**, 1187–1192 (2017).
16. Geim, A. K. & Grigorieva, I. V. Van der Waals heterostructures. *Nature* **499**, 419–425 (2013).
17. Dean, C. R. et al. Hofstadter's butterfly and the fractal quantum Hall effect in moiré superlattices. *Nature* **497**, 598–602 (2013).
18. Balents, L., Dean, C. R., Efetov, D. K. & Young, A. F. Superconductivity and strong correlations in moiré flat bands. *Nat. Phys.* **16**, 725–733 (2020).
19. Cao, Y. et al. Unconventional superconductivity in magic-angle graphene superlattices. *Nature* **556**, 43–50 (2018).
20. Cao, Y. et al. Correlated insulator behaviour at half-filling in magic-angle graphene superlattices. *Nature* **556**, 80–84 (2018).
21. Yankowitz, M. et al. Tuning superconductivity in twisted bilayer graphene. *Science* **363**, 1059–1064 (2019).
22. Sharpe, A. L. et al. Emergent ferromagnetism near three-quarters filling in twisted bilayer graphene. *Science* **365**, 605–608 (2019).
23. Lu, X. et al. Superconductors, orbital magnets and correlated states in magic-angle bilayer graphene. *Nature* **574**, 653–657 (2019).
24. Bistritzer, R. & MacDonald, A. H. Moiré bands in twisted double-layer graphene. *Proc. Natl Acad. Sci. USA* **108**, 12233–12237 (2011).
25. Utama, M. I. B. et al. Visualization of the flat electronic band in twisted bilayer graphene near the magic angle twist. *Nat. Phys.* **17**, 184–188 (2021).
26. Wang, L. et al. Correlated electronic phases in twisted bilayer transition metal dichalcogenides. *Nat. Mater.* **19**, 861–866 (2020).
27. Alden, J. S. et al. Strain solitons and topological defects in bilayer graphene. *Proc. Natl Acad. Sci. USA* **110**, 11256–11260 (2013).
28. Jiang, Z. et al. MoS_2 moiré superlattice for hydrogen evolution reaction. *ACS Energy Lett.* **4**, 2830–2835 (2019).
29. Ding, Y. et al. Stacking modes-induced chemical reactivity differences on chemical vapor deposition-grown trilayer graphene. *ACS Appl. Mater. Interfaces* **10**, 23424–23431 (2018).
30. Ding, Y. et al. Stacking-mode-induced reactivity enhancement for twisted bilayer graphene. *Chem. Mater.* **28**, 1034–1039 (2016).
31. Yoo, H. et al. Atomic and electronic reconstruction at the van der Waals interface in twisted bilayer graphene. *Nat. Mater.* **18**, 448–453 (2019).
32. Kerelsky, A. et al. Maximized electron interactions at the magic angle in twisted bilayer graphene. *Nature* **572**, 95–100 (2019).
33. Kazmierczak, N. P. et al. Strain fields in twisted bilayer graphene. *Nat. Mater.* **20**, 956–963 (2021).
34. Trambly de Laissardière, G., Mayou, D. & Magaud, L. Localization of Dirac electrons in rotated graphene bilayers. *Nano Lett.* **10**, 804–808 (2010).
35. Bentley, C. L., Kang, M. & Unwin, P. R. Nanoscale surface structure–activity in electrochemistry and electrocatalysis. *J. Am. Chem. Soc.* **141**, 2179–2193 (2019).
36. Unwin, P. R., Güell, A. G. & Zhang, G. Nanoscale electrochemistry of sp^2 carbon materials: from graphite and graphene to carbon nanotubes. *Acc. Chem. Res.* **49**, 2041–2048 (2016).
37. Schmickler, W. & Santos, E. *Interfacial Electrochemistry* 2nd edn (Springer, 2010).
38. Bard, A. J. & Faulkner, L. R. *Electrochemical Methods: Fundamentals and Applications* 2nd edn (Wiley, 2001).
39. Li, J., Pham, P. H. Q., Zhou, W., Pham, T. D. & Burke, P. J. Carbon-nanotube–electrolyte interface: quantum and electric double layer capacitance. *ACS Nano* **12**, 9763–9774 (2018).
40. Heller, I., Kong, J., Williams, K. A., Dekker, C. & Lemay, S. G. Electrochemistry at single-walled carbon nanotubes: the role of band structure and quantum capacitance. *J. Am. Chem. Soc.* **128**, 7353–7359 (2006).
41. Henstridge, M. C., Laborda, E., Rees, N. V. & Compton, R. G. Marcus–Hush–Chidsey theory of electron transfer applied to voltammetry: a review. *Electrochim. Acta* **84**, 12–20 (2012).
42. Kurchin, R. & Viswanathan, V. Marcus–Hush–Chidsey kinetics at electrode–electrolyte interfaces. *J. Chem. Phys.* **153**, 134706 (2020).
43. Bae, J. H., Yu, Y. & Mirkin, M. V. Diffuse layer effect on electron-transfer kinetics measured by scanning electrochemical microscopy (SECM). *J. Phys. Chem. Lett.* **8**, 1338–1342 (2017).
44. Fan, L., Liu, Y., Xiong, J., White, H. S. & Chen, S. Electron-transfer kinetics and electric double layer effects in nanometer-wide thin-layer cells. *ACS Nano* **8**, 10426–10436 (2014).
45. Zhang, K. & Tadmor, E. B. Structural and electron diffraction scaling of twisted graphene bilayers. *J. Mech. Phys. Solids* **112**, 225–238 (2018).
46. Pavlov, S. V., Nazmutdinov, R. R., Fedorov, M. V. & Kislenko, S. A. Role of graphene edges in the electron transfer kinetics: insight from theory and molecular modeling. *J. Phys. Chem. C* **123**, 6627–6634 (2019).

Methods

Chemicals and materials. Natural Kish graphite crystals were purchased from Graphene Supermarket. Si/SiO$_2$ wafers (0.5 mm thick with 285 nm SiO$_2$) and polydimethylsiloxane stamps were purchased from NOVA Electronic Materials and MTI Corporation, respectively. Sn/In alloy was purchased from Custom Thermoelectric. Poly(bisphenol-A carbonate), hexaammineruthenium(III) chloride (98%), ferrocenemethanol (97%), cobalt(II) chloride hexahydrate (98%), 1,10-phenanthroline (>99%), potassium chloride (>99%) and 4-nitrobenzenediazonium tetrafluoroborate (97%) were purchased from Sigma-Aldrich and used as received. Sulfuric acid (ACS grade, 95–98%) was used as received from Lab Chem (Fisher Scientific). All aqueous electrolyte solutions were prepared with type I water (EMD Millipore, 18.2 MΩ cm resistivity). The 2 mM solutions of tris(1,10-phenanthroline)cobalt(II) were prepared by dissolving 1:3 molar ratios of solid cobalt(II) chloride and 1,10-phenanthroline in water. In Ru(NH$_3$)$_6$$^{3+}$ and Co(phen)$_3$$^{2+}$ solutions, solid KCl was added as a supporting electrolyte for a concentration of 100 mM.

Sample fabrication. Graphene and boron nitride (hBN) flakes were mechanically exfoliated onto SiO$_2$ (285 nm)/Si substrates from their bulk crystals using the well-established 'scotch tape' method. Individual graphene flakes at SiO$_2$/Si chips were located by optical microscopy (Supplementary Fig. 15a,b). The number of layers was identified by the optical contrast and further verified by Raman spectroscopy (HORIBA LabRAM Evo). Supplementary Fig. 15c,d shows optical contrast (green channel) of ~7% and ~14% at the graphene flake region, indicating a graphene monolayer and bilayer, respectively[47]. Raman measurements were performed using a 532 nm excitation and a ×100 objective lens for a minimized laser spot. The shape of the 2D band (2,600–2,750 cm^{-1}) was used to determine the number of graphene layers. Supplementary Fig. 15e,f shows the 2D bands presented as a sharp Lorentzian peak with a full-width at half-maximum of ~25 cm^{-1} (monolayer) and a broad peak (with four components) with a full-width at half-maximum of ~55 cm^{-1} (bilayer)[48].

TBG samples were prepared using the 'tear and stack' technique[20] on a temperature-controlled heating stage (Instec) equipped with an optical microscope (Mitutoyo FS70) and a micromanipulator (MP-285, Sutter Instrument). A thin poly(bisphenol-A carbonate) film attached to a polydimethylsiloxane stamp was used to pick up individual hBN flakes (10–20 nm thick) on the SiO$_2$/Si substrate. The picked-up hBN was aligned with half of a graphene monolayer, which was then torn along the edge of the hBN. The stage was rotated to a desired moiré twist angle (θ_m), and then the picked-up graphene was placed over the remaining portion of the graphene to form the TBG/hBN heterostructure. A thick graphite flake (10–100 nm thick) was then picked up to partially overlap with the graphene to form the immediate electrical contact to the TBG. The poly(bisphenol-A carbonate) film was then delaminated from the polydimethylsiloxane stamp and placed onto a fresh SiO$_2$/Si chip. Sn/In contacts were made to the graphite contact using the micro-soldering method[49].

The Raman spectra of the TBG/hBN heterostructures were obtained to verify the absence of structural defects at the graphene surface, which are known to enhance the DOS[10]. No disorder peaks (for example, D-band, 1,350 cm^{-1}) were found in the spectra of the fabricated samples (Supplementary Fig. 16). Atomic force microscopy was used to characterize the topography of the exposed graphene surfaces in the TBG/hBN heterostructures (Supplementary Fig. 1). The fabricated samples show atomically flat, pristine surfaces for electrochemical measurements.

STM and electron microscopy measurements. STM measurements were carried out with a Park NX10 STM module (Park System) operated in ambient conditions (that is, room temperature, 1 atm pressure). Pt–Ir tips used for imaging were fabricated via electrochemical etching of 0.25 mm Pt–Ir wires in saturated CaCl$_2$ solutions. Constant-current images were taken with a 0.1 V tip–sample bias and a 100 pA set point. The transmission electron microscopy images of the nanopipettes (Supplementary Figs. 6 and 21) were obtained with a JEOL 1200EX transmission electron microscope operated at 100 keV. The ~1 mm portion of the pipette was attached to the grid (PELCO Hole Grids) such that the pipette tip is positioned in the centre hole, and the rest of the pipette was cut off. Selected area electron diffraction patterns were collected on an FEI Tecnai T20 S-TWIN transmission electron microscope with a LaB$_6$ filament operated at 200 kV. Selected area electron diffraction was used to resolve the twist angles for samples with $\theta_m > 5°$. To obtain the diffraction patterns, the fabricated TBG/hBN samples were transferred onto a holey silicon nitride membrane after electrochemical measurements.

SECCM measurements. The SECCM probes were single-channel nanopipettes pulled from quartz capillaries (inner diamter, 0.7 mm; outer diameter, 1 mm) using a laser puller (P-2000, Sutter Instrument), yielding orifices with sizes of 50–500 nm. The dimensions and geometries of the probes were determined by transmission electron microscopy, as presented in Supplementary Figs. 6 and 21. The nanopipettes were filled with the electrolyte solution containing the redox species. Silver wires coated with AgCl were inserted into the channels of nanopipettes and used as quasi-counter/reference electrodes. The SECCM experiments were performed using a Park NX10 SICM Module (Park Systems). The nanopipette was positioned over the area of interest aided by an optical microscope, and then

it slowly approached the sample (at 100 nm s^{-1}) until a current >2 pA was detected due to the contact between the meniscus and the sample surface. A bias was held at a potential where the reaction takes place in a diffusion-limited rate (–0.5 V versus Ag/AgCl for Ru(NH$_3$)$_6$$^{3+}$ and 0.5 V versus Ag/AgCl for Co(Phen)$_3$$^{2+}$) during the approach. The local cyclic voltammograms were subsequently recorded at various locations on the sample surface. In steady-state voltammograms, the half-wave potential, $E_{1/2}$, is defined as the potential at $i = i_\infty/2$, where i_∞ is the diffusion-limited current plateau. For diazonium deposition on graphite (Supplementary Fig. 22), which was used to confirm that nanopipette sizes measured by transmission electron microscopy were representative of the meniscus contact area (as demonstrated previously[50,51]), deposition was performed using a nanopipette filled with 0.1 mM 4-nitrobenzenediazonium tetrafluoroborate in 50 mM H$_2$SO$_4$ solution and with a constant bias of –0.2 V versus Ag/AgCl for 20 seconds.

Calculation of DOS. The DOS for TBG was calculated as a function of θ_m using the ab initio perturbation continuum model developed previously[52]. The model incorporates in-plane and out-of-plane relaxation effects as correction terms to intra-layer Dirac Hamiltonians and interlayer coupling terms, respectively[53]. The low-energy electronic structure is based on a momentum expansion about the valley K point of the supercell Brillouin zone, allowing a smooth dependence of bands on the twist angle, for $0.18° < \theta_m < 6°$. Previous work[52,54] shows that the perturbation continuum model exactly reproduces results of the more expensive ab initio tight-binding model[55], and both are in good agreement with full density functional theory (DFT) calculations[56]. The energy range of integration for the DOS was fixed at ±0.7 eV around the CNP. For evaluation of the LDOS, the normalized moiré supercell was divided into a 90×90 grid in real space and sampled over 36 k points in the Brillouin zone. We kept the sublattice symmetry intact and assumed no extra screening of the interlayer coupling constants. The Fermi velocity, however, was increased by 20%, since DFT calculations of graphene without GW screening corrections are known to overestimate the experimental Fermi velocity by roughly 20% (ref. [32]). The DOS of $\theta_m = 0°$ was obtained from calculations of a single bilayer unit cell with Bernal stacking, employing the same DFT-based tight-binding model as the twisted structures[55].

Determination of moiré angles and uniaxial heterostrain. The real-space moiré wavelengths, λ_m, and corresponding moiré twist angles, θ_m, were obtained from the STM images by fitting the tunnelling intensities to a linear combination of bivariate Gaussians. The mesh was constructed by performing Delaunay triangulation on the Gaussian centres (Supplementary Fig. 2), enabling us to measure the three sides of each moiré triangle, $\lambda_i = \lambda_1, \lambda_2$ or λ_3. The local twist angles and uniaxial heterostrain are measured through their effects on the moiré patterns using a methodology described previously[32], as summarized below.

We consider, without loss of generality, the case where one of the two monolayers has been twisted by θ_t and the other is subject to a uniaxial heterostrain along the direction θ_s from the x axis. The reciprocal lattice vectors of the twisted layer are related to the original reciprocal lattice vectors {k_1, k_2, k_3} by a rotation matrix:

$$\mathbf{k}_i^{\text{twisted}} = \begin{bmatrix} \cos\theta_t & -\sin\theta_t \\ \sin\theta_t & \cos\theta_t \end{bmatrix} \mathbf{k}_i \tag{6}$$

Likewise, the reciprocal lattice vectors of the strained layer are related to the original k_i by a strain matrix, which is given below in terms of the percent strain ε and the Poisson ratio of graphene δ (for which we use $\delta = 0.16$), and a series of rotation matrices to account for angle of strain application θ_s:

$$\mathbf{k}_i^{\text{strained}} = \begin{bmatrix} \cos\theta_s & \sin\theta_s \\ -\sin\theta_s & \cos\theta_s \end{bmatrix} \begin{bmatrix} \frac{1}{1+\epsilon} & 0 \\ 0 & \frac{1}{1-\delta\epsilon} \end{bmatrix} \begin{bmatrix} \cos\theta_s & -\sin\theta_s \\ \sin\theta_s & \cos\theta_s \end{bmatrix} \mathbf{k}_i \tag{7}$$

In the case where one layer has been twisted and the other has been strained as so, the moiré reciprocal wavelengths

$$\mathbf{L}_i^k = \left| \mathbf{k}_i^{\text{twisted}} - \mathbf{k}_i^{\text{strained}} \right| \tag{8}$$

are expressed in terms of θ_t, θ_s, ε and the monolayer k_i. The set of three experimentally accessible real-space moiré wavelengths, λ_i, are related to the reciprocal wavelengths by a Fourier transform:

$$\lambda_i = 4\pi / \left(\sqrt{3} \mathbf{L}_i^k \right) \tag{9}$$

The resultant set of equations are solved numerically using nonlinear least squares to determine θ_t, θ_s and ε from the experimental {$\lambda_1, \lambda_2, \lambda_3$}.

The histograms of the extracted local twist angles (θ_m or θ_t) and uniaxial heterostrain (ε) are shown in Supplementary Figs. 3 and 4, respectively, and Supplementary Table 1 tabulates these values for all samples. In a few cases (samples 6, 11 and 12), Delaunay triangulation could not triangulate the moiré superlattice patterns. For samples 6 and 11, manually drawn line profiles were used to determine the periodicity of the AA stacking sites from which θ_m could

be determined (but not ε). For sample 12, selected area electron diffraction (Supplementary Fig. 18) was used to determine θ_m.

The effects of ε on the band structure are generally less pronounced than the effects of θ_m (refs. [57,58]). Accordingly, while even small changes in ε may introduce notable changes to the correlated electronic phases that emerge at low temperatures[58], we infer that the effects of small variations in ε on interfacial charge transfer are undetectable in our experiments for the range of heterostrain observed in our samples ($\varepsilon \leq 1.1\%$). However, it is conceivable that much higher values of heterostrain may perturb charge transfer kinetics appreciably[12].

Calculation of quantum capacitance. The quantum capacitance describes the variation of the electrical charge with respect to the change of chemical potential, and it has a strong dependence on the electronic structure of the material. C_q is related to the chemical potential (V_q) of the electron. Theoretical C_q values as a function of V_q for TBG are calculated using the equations below[59]:

$$C_q = e^2 \int_{-\infty}^{+\infty} D(\epsilon) F_T(\epsilon - eV_q) \, d\epsilon \tag{10}$$

$$F_T(\epsilon) = (4k_B T)^{-1} \operatorname{sech}^2(\epsilon/2k_B T) \tag{11}$$

where $D(\epsilon)$ is the density of states, which we centre at the CNP, and $F_T(\epsilon)$ is the thermal broadening function; k_B is Boltzmann's constant, and we take T to be 300 K.

The compact layer capacitance in aqueous solution is $10-20\,\mu\text{F cm}^{-2}$, independent of the ionic strength[60]. The diffuse-layer capacitance is $>100\,\mu\text{F cm}^{-2}$ in 0.1 M KCl solution[38]. The total electric double-layer capacitance is governed by the compact layer capacitance, and we use a constant $C_{dl} = 10\,\mu\text{F cm}^{-2}$ to simplify the calculation. By numerically solving the self-consistent equations relating V_{app}, V_q, V_{dl}, C_q and C_{dl} using Simpson integration and nonlinear least squares

$$V_{app} = V_{dl} + V_q \tag{12}$$

$$\frac{V_{dl}}{V_q} = \frac{C_q}{C_{dl}} \tag{13}$$

we obtain the relationship of V_{dl} and V_{app} shown in Fig. 2c. The same procedure was followed to calculate the local C_q versus V_q dependence and the V_{dl} versus V_{app} dependence at different stacking regions in a graphene bilayer superlattice, as shown in Supplementary Fig. 19.

In situ conductance measurements. The in situ conductance measurement was implemented using a bipotentiostat (CHI 760E, CH Instruments). Graphite was used to make contact to two ends of a graphene flake as shown in Extended Data Fig. 2a with InSn microsolder forming contact to the graphite. To ensure that only the graphene surface is electrochemically gated, a micropipette (20–30 μm in diameter) filled with electrolyte was used to selectively wet the sample surface (Extended Data Fig. 2b). Two similar electrochemical potentials (V_1 and V_2) were applied, one to each of the two graphite contacts. The potential difference ($V_1 - V_2$) was held constant to induce a cross-conduction current (i_c) across the flake. The currents flowing at both channels (i_1 and i_2) were then determined by both the Faradaic current (i_F) and i_c. The i_c was evaluated using the equation below:

$$i_c = (i_1 - i_2)/2 \tag{14}$$

The flake resistance was calculated as $R = (V_1 - V_2)/i_c$. The observed resistance maximum represents the charge neutrality point of bilayer graphene (–0.18 to –0.13 V versus Ag/AgCl, or 0.07 to 0.12 V versus E^0 of $\text{Ru(NH}_3)_6^{3+/2+}$ shown in Extended Data Fig. 2c).

Calculation of the rate constant. Electrochemical rate constants were calculated using the Marcus–Hush–Chidsey formalism, and extension incorporating the electronic states by Kurchin and Viswanathan[42]:

$$k_{ox} \propto \int D(\epsilon - eV_q) \exp\left[-\frac{(\lambda - E^0 + \epsilon)^2}{4\lambda k_B T}\right] \frac{\exp\left(\frac{\epsilon}{k_B T}\right)}{1 + \exp\left(\frac{\epsilon}{k_B T}\right)} d\epsilon \tag{15}$$

$$k_{red} \propto \int D(\epsilon - eV_q) \exp\left[-\frac{(\lambda + E^0 - \epsilon)^2}{4\lambda k_B T}\right] \frac{d\epsilon}{1 + \exp\left(\frac{\epsilon}{k_B T}\right)} \tag{16}$$

where $\lambda = 0.82$ eV is the reorganization energy for the $\text{Ru(NH}_3)_6^{3+/2+}$ redox couple[14], E^0 is the energy level of the formal potential, k_B is the Boltzmann constant and $D(\epsilon)$ is the DOS. We assume that the DOS is aligned with the molecular energy levels such that

$\epsilon_F = 0$, and the alignment is shifted by eV_q due to the effects of quantum capacitance. The charge neutrality point of bilayer graphene relative to E^0 is determined from in situ conductance measurements described in Extended Data Fig. 2.

Finite-element simulations. The finite-element simulations were performed using COMSOL Multiphysics v.5.4 (COMSOL) to model the voltammetric responses. Simulation details and procedures of determining kinetic parameters are provided in Supplementary Section 1.

Data availability
The data supporting the findings of this study are available within the Article and its Supplementary Information files. Source data are provided with this paper. Any additional data are available from the corresponding author.

Code availability
The computer codes used for Delaunay triangulation and quantum capacitance calculations are publicly available at https://github.com/bediakolab/bediakolab_scripts. The computer code used for tight-binding band structure calculations of TBG is publicly available at https://github.com/stcarr/kp_tblg. The computer code used for calculation of theoretical electrochemical rate constants is available in the Github package for calculating Marcus–Hush–Chidsey reaction kinetics incorporating DOS: https://github.com/aced-differentiate/MHC_DOS.

References
47. Li, H. et al. Rapid and reliable thickness identification of two-dimensional nanosheets using optical microscopy. *ACS Nano* **7**, 10344–10353 (2013).
48. Ferrari, A. C. et al. Raman spectrum of graphene and graphene layers. *Phys. Rev. Lett.* **97**, 187401 (2006).
49. Girit, Ç. Ö. & Zettl, A. Soldering to a single atomic layer. *Appl. Phys. Lett.* **91**, 193512 (2007).
50. Kirkman, P. M. et al. Spatial and temporal control of the diazonium modification of sp² carbon surfaces. *J. Am. Chem. Soc.* **136**, 36–39 (2014).
51. Patel, A. N., McKelvey, K. & Unwin, P. R. Nanoscale electrochemical patterning reveals the active sites for catechol oxidation at graphite surfaces. *J. Am. Chem. Soc.* **134**, 20246–20249 (2012).
52. Carr, S., Fang, S., Zhu, Z. & Kaxiras, E. Exact continuum model for low-energy electronic states of twisted bilayer graphene. *Phys. Rev. Res.* **1**, 013001 (2019).
53. Carr, S. et al. Relaxation and domain formation in incommensurate two-dimensional heterostructures. *Phys. Rev. B* **98**, 224102 (2018).
54. Carr, S., Fang, S. & Kaxiras, E. Electronic-structure methods for twisted moiré layers. *Nat. Rev. Mater.* **5**, 748–763 (2020).
55. Fang, S. & Kaxiras, E. Electronic structure theory of weakly interacting bilayers. *Phys. Rev. B* **93**, 235153 (2016).
56. Lucignano, P., Alfè, D., Cataudella, V., Ninno, D. & Cantele, G. Crucial role of atomic corrugation on the flat bands and energy gaps of twisted bilayer graphene at the magic angle $\theta \sim 1.08°$. *Phys. Rev. B* **99**, 195419 (2019).
57. Huder, L. et al. Electronic spectrum of twisted graphene layers under heterostrain. *Phys. Rev. Lett.* **120**, 156405 (2018).
58. Bi, Z., Yuan, N. F. Q. & Fu, L. Designing flat bands by strain. *Phys. Rev. B* **100**, 035448 (2019).
59. Yang, G. M., Zhang, H. Z., Fan, X. F. & Zheng, W. T. Density functional theory calculations for the quantum capacitance performance of graphene-based electrode material. *J. Phys. Chem. C* **119**, 6464–6470 (2015).
60. Xia, J., Chen, F., Li, J. & Tao, N. Measurement of the quantum capacitance of graphene. *Nat. Nanotechnol.* **4**, 505–509 (2009).

Acknowledgements

Author contributions

Competing interests

Additional information
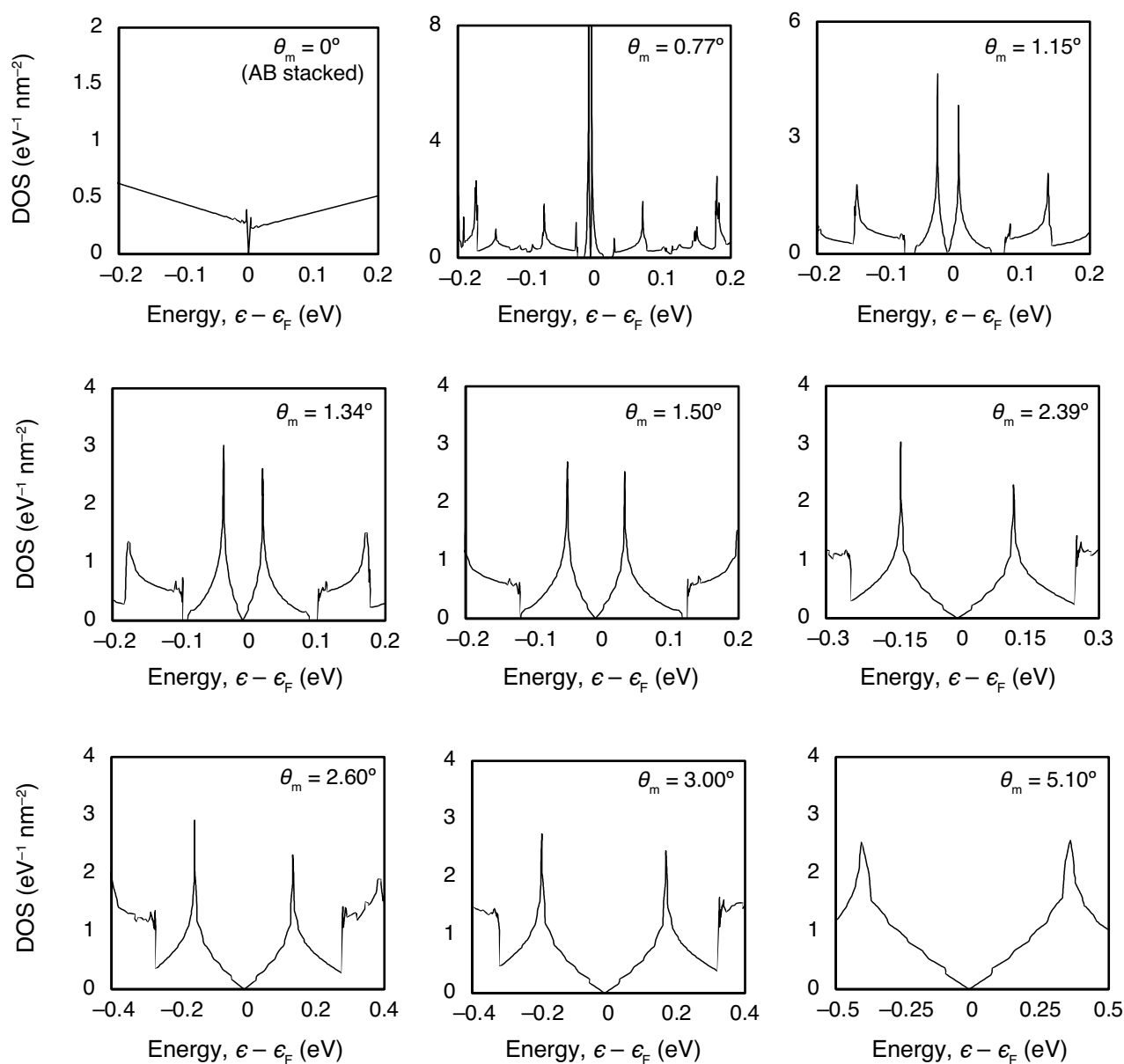
Extended Data Fig. 1 | DOS of twisted bilayer graphene. Calculated DOS of twisted bilayer graphene with various moiré twist angles, θ_m. $\theta_m = 0°$ corresponds to Bernal (AB) stacked bilayer graphene.

a

50 μm

b

micropipette

electrolyte

Ag/AgCl

graphite

graphite

$V_1 = V_{app} - \Delta V$

$V_2 = V_{app} + \Delta V$

A i_1

i_2 A

SiO$_2$

Si

PC film

hBN

graphene

c

$E^0 (Ru(NH_3)_6^{2+/3+})$ $E^0 (Co(Phen)_3^{2+/3+})$

$E^0 (FcMeOH^{0/+})$

R/R_{max}

V_{app} *vs.* Ag/AgCl (V)
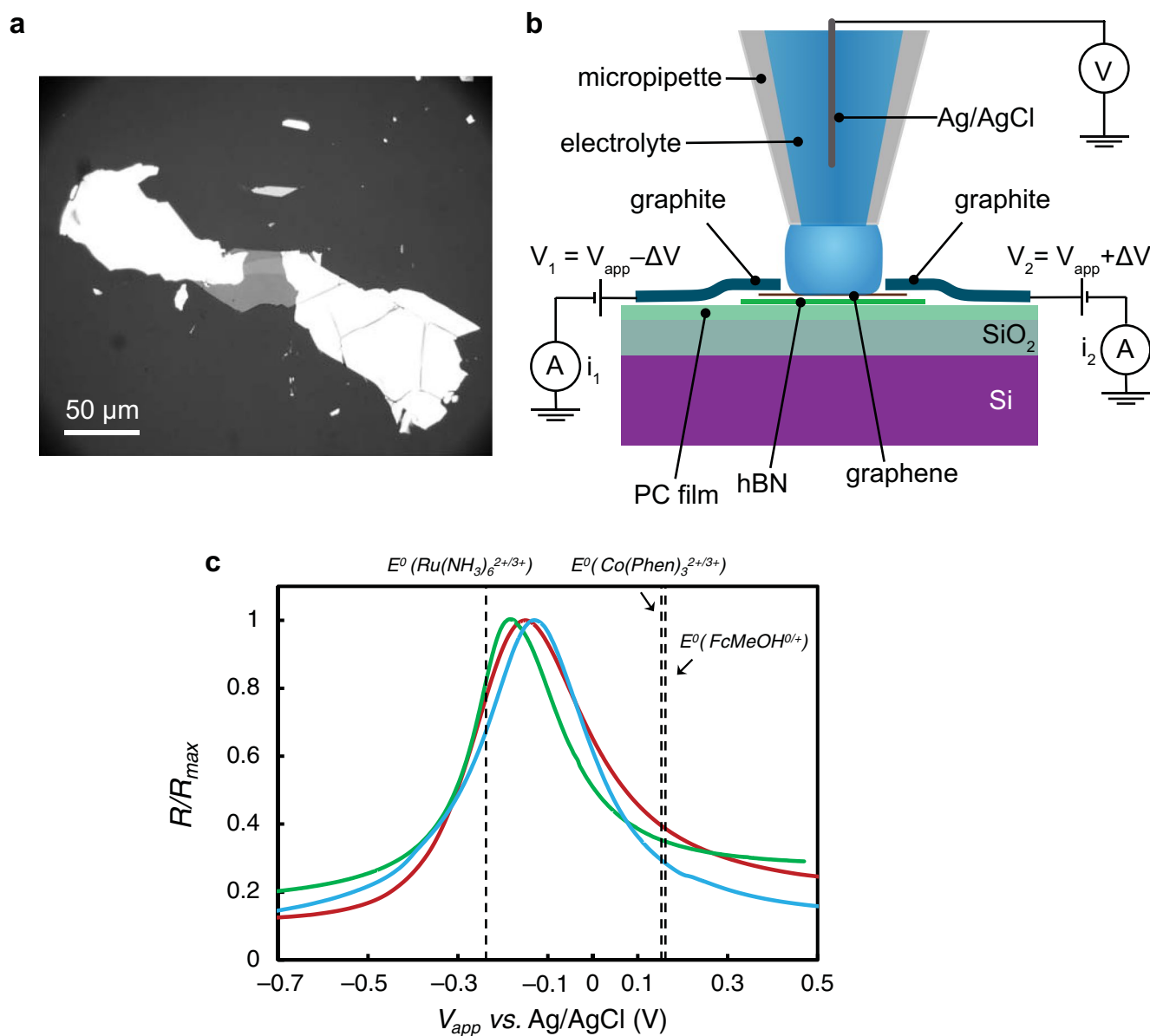
Extended Data Fig. 2 | *In situ* conductance measurements of bilayer graphene as a function of the electrochemical bias. a, Optical micrograph of representative device for *in situ* conductance measurements. **b**, Schematic of conductance measurement. The micropipettes are filled with 2 mM Ru(NH$_3$)$_6$$^{3+}$ in 0.1 M KCl aqueous solution. **c**, Flake resistance as a function of the electrochemical bias obtained from 3 different AB-stacked bilayer graphene samples, showing the position of the charge neutrality point (maximum resistance) relative to the E^0 values of the three redox couples interrogated in this study.
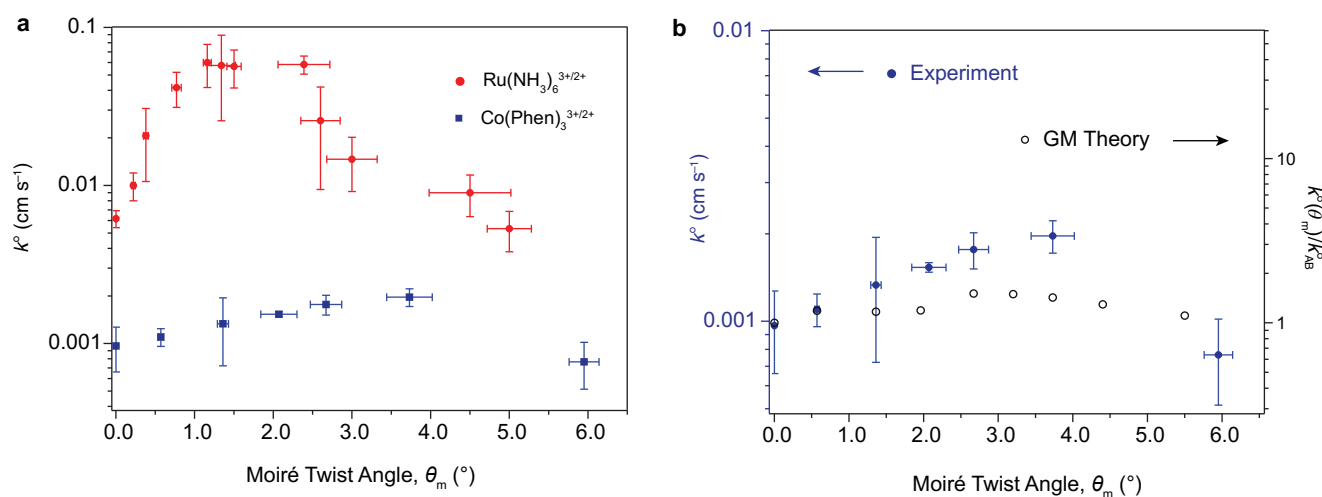
Extended Data Fig. 3 | Moiré angle dependent electron transfer rate of Ru(NH₃)₆³⁺/²⁺ and Co(Phen)₃³⁺/²⁺. **a**, $k°$ extracted from the experimental voltammograms as a function of twist angle for the Co(Phen)₃³⁺/²⁺ (blue squares) and Ru(NH₃)₆³⁺/²⁺ (red circles) redox couples. **b**, $k°$ for Co(Phen)₃³⁺/²⁺ extracted from the experimental voltammograms (blue filled circles) as a function of twist angle compared to the values calculated with GM framework (black open circles). The horizontal and vertical error bars represent the standard deviations of θ_m and $k°$, respectively.